Geochemistry Geophysics Geosystems G3

Article
Volume 13, Number 10
6 December 2012
Q10Z51, doi:10.1029/2012GC004384
ISSN: 1525-2027

Published by AGU and the Geochemical Society

Magnetic anisotropy, magnetostatic interactions and identification of magnetofossils

Jinhua Li, Wenfang Wu, Qingsong Liu, and Yongxin Pan

Paleomagnetism and Geochronology Laboratory, Key Laboratory of Earth's Deep Interior, Institute of Geology and Geophysics, Chinese Academy of Sciences, Beijing 100029, China

France-China Biomineralization and Nano-structure Laboratory, Chinese Academy of Sciences, Beijing 100029, China

[1] Single-domain magnetite particles produced by magnetotactic bacteria (MTB) and aligned in chains, called magnetosomes, are potentially important recorders of paleomagnetic, paleoenvironmental and paleolife signals. Rock magnetic properties related to the anisotropy of magnetosome chains have been widely used to identify fossilized magnetosomes (magnetofossils) preserved in geological materials. However, ambiguities exist when linking magnetic properties to the chain structure because of the complexity of chain integrity and magnetostatic interactions among magnetofossils that results from chain collapse during post-depositional diagenesis. In this paper, magnetic properties of three sets of samples containing extracted magnetosomes of the cultured *Magnetospirillum magneticum* strain AMB-1 were analyzed to determine how chain integrity and particle concentration influence magnetic properties. Intact MTB and well-dispersed magnetosome chains are characterized by strong magnetic anisotropy and weak magnetostatic interactions, but progressive chain breakup and particle clumping significantly increase the degree of magnetostatic interaction. This results in a change of the magnetic signature toward properties typical of interacting, single-domain particles, i.e., a decrease of the ratio of anhysteretic remanent magnetization to the saturation isothermal remanent magnetization, decreasing in the crossing point of the Wohlfarth-Cisowski test and in the delta ratio between losses of field and zero-field cooled remanent magnetization across the Verwey transition, as well as vertical broadening of the first-order reversal curve distribution. We propose a new diagram that summarizes the Verwey transition properties, with diagnostic limits for intact and collapsed chains of magnetosomes. This diagram can be used, in conjunction with other parameters, to identify unoxidized magnetofossils in sediments and rocks.

Components: 8500 words, 9 figures, 2 tables.

Keywords: δ-plot; FORC; magnetic anisotropy; magnetofossils; magnetostatic interaction; magnetotactic bacteria.

Index Terms: 1505 Geomagnetism and Paleomagnetism: Biogenic magnetic minerals; 1512 Geomagnetism and Paleomagnetism: Environmental magnetism; 1540 Geomagnetism and Paleomagnetism: Rock and mineral magnetism.

Received 10 August 2012; **Revised** 22 October 2012; **Accepted** 26 October 2012; **Published** 6 December 2012.

Li, J., W. Wu, Q. Liu, and Y. Pan (2012), Magnetic anisotropy, magnetostatic interactions and identification of magnetofossils, *Geochem. Geophys. Geosyst.*, *13*, Q10Z51, doi:10.1029/2012GC004384.

Theme: Magnetism From Atomic to Planetary Scales: Physical Principles and Interdisciplinary Applications in Geosciences and Planetary Sciences

1. Introduction

[2] Single-domain (SD) magnetite crystals formed within membrane organelles by magnetotactic bacteria (MTB), called magnetosomes, have long been of interest in the bio- and geo-sciences, including paleomagnetic, paleoenvironmental and paleolife studies [*Kopp and Kirschvink*, 2008; *Jimenez-Lopez et al.*, 2010]. In MTB cells, magnetosomes are often organized into single or multiple chains that facilitate orientation and navigation of cells along geomagnetic field lines, a process known as magnetotaxis [*Bazylinski and Frankel*, 2004; *Faivre and Schüler*, 2008]. After cell death and dissolution, magnetosome crystals can be preserved in sediments and are then called magnetofossils [*Chang and Kirschvink*, 1989; *Kopp and Kirschvink*, 2008]. Since MTB communities and their synthesized magnetites are sensitive to environmental factors such as oxygen, salinity, iron source and nitrate [*Petermann and Bleil*, 1993; *Bazylinski et al.*, 2004; *Simmons et al.*, 2004; *Flies et al.*, 2005; *Li and Pan*, 2012; *Lin et al.*, 2012], magnetofossils in natural systems bear useful paleoecological and paleoenvironmental information [*Hesse*, 1994; *Yamazaki and Kawahata*, 1998; *Kim et al.*, 2005; *Kopp et al.*, 2007; *Schumann et al.*, 2008; *Roberts et al.*, 2011; *Larrasoaña et al.*, 2012; *Yamazaki*, 2012]. Furthermore, magnetofossils can serve as stable carriers of natural remanent magnetization (NRM) [*Chang and Kirschvink*, 1989; *Pan et al.*, 2005a; *Kopp and Kirschvink*, 2008], and as potential biomarkers for early terrestrial and extraterrestrial life [*Thomas-Keprta et al.*, 2002; *Jimenez-Lopez et al.*, 2010].

[3] The distinctive features of magnetosome magnetite, including the uniform SD-size range, narrow and negatively skewed grain-size distributions, distinctive crystal morphology and chain structure, make it feasible to identify magnetofossils in natural materials through combination of electron microscopy and magnetic methods [*Yamazaki and Kawahata*, 1998; *Weiss et al.*, 2004a, 2004b; *Kim et al.*, 2005; *Pan et al.*, 2005a; *Housen and Moskowitz*, 2006; *Kopp and Kirschvink*, 2008; *Schumann et al.*, 2008; *Kopp et al.*, 2009; *Roberts et al.*, 2011, 2012; *Yamazaki*, 2012]. Specifically, rock magnetic methods are useful for rapid screening of large quantities of geological samples for magnetofossils [*Petersen et al.*, 1986; *Moskowitz et al.*, 1993; *Egli*, 2004a, 2004b, 2004c; *Egli et al.*, 2010; *Kim et al.*, 2005; *Pan et al.*, 2005a; *Housen and Moskowitz*, 2006; *Kind et al.*, 2011; *Roberts et al.*, 2011, 2012]. Intact MTB and well-dispersed magnetosome chains are characterized by strong magnetic anisotropy and weak magnetostatic interactions. Combination of these characteristics has been used to identify magnetofossils by various rock magnetic parameters, such as the ratio of the anhysteretic remanent magnetization (ARM) to the isothermal remanent magnetization (IRM) [*Petersen et al.*, 1986; *Moskowitz et al.*, 1993; *Egli*, 2004a, 2004b, 2004c], coercivity spectra [*Egli*, 2004a, 2004b, 2004c; *Pan et al.*, 2005a], and first-order reversal curve (FORC) analyses [*Chen et al.*, 2007; *Egli et al.*, 2010; *Kind et al.*, 2011; *Roberts et al.*, 2011, 2012], and low-temperature magnetization measurements [*Moskowitz et al.*, 1993; *Carter-Stiglitz et al.*, 2002; *Weiss et al.*, 2004a; *Pan et al.*, 2005a; *Housen and Moskowitz*, 2006], and ferromagnetic resonance (FMR) spectra [*Weiss et al.*, 2004a; *Kopp et al.*, 2006a, 2006b; *Fischer et al.*, 2008; *Gehring et al.*, 2011; *Kind et al.*, 2011; *Roberts et al.*, 2011, 2012].

[4] Intact magnetosome chains often acquire a significantly enhanced low-temperature saturation IRM (SIRM) when cooling the sample across the Verwey transition in a strong field (FC) compared to cooling in zero field (ZFC), which results in an apparent bifurcation of zero-field-warming SIRM curves between FC and ZFC below the Verwey transition [*Moskowitz et al.*, 1993]. The δ-ratio ($\delta = \delta_{FC}/\delta_{ZFC}$) quantifies the difference between the remanence losses of FC (δ_{FC}) and ZFC (δ_{ZFC}) curves upon warming through the Verwey transition [*Moskowitz et al.*, 1993], where the δ-ratio exceeds 2 for intact magnetosome chains [*Moskowitz et al.*, 1993, 2008; *Pan et al.*, 2005b; *Li et al.*, 2009, 2010a, 2010b].

[5] Identification and quantification of magnetofossils in sediments and rocks is, nevertheless, not straightforward because chain fragmentation, and collapse and aggregation of magnetosomes during post-depositional processes may alter the original bulk magnetic signature, and magnetofossils often occur in mixtures with abiogenic magnetic minerals [e.g., *Kopp and Kirschvink*, 2008]. Therefore, it is essential to evaluate the effects of magnetosome chain disruption on the bulk magnetic properties. *Moskowitz et al.* [1988, 1993] found that the lysed (broken) magnetosome chains, compared with intact MTB cells, have relatively reduced values of coercivity, remanence coercivity, remanence ratio and ARM/IRM. *Kobayashi et al.* [2006] demonstrated that these values gradually decrease with increasing chain collapse. Recently, *Li et al.* [2010a] showed that lysed chains are characterized by lower δ-ratio and larger δ_{ZFC} values, as well as an increased vertical spread of the FORC distribution. These experimental studies suggest that the chain structure of

magnetosomes plays an important role in contributing to the unique magnetic properties of magnetosomes (magnetofossils). However, knowledge about magnetic anisotropy and magnetostatic interactions of magnetosomes remains sparse, and systematic studies of the bulk magnetic properties of magnetosomes with different degrees of chain integrity and particle concentration are needed.

[6] In this study, we carried out detailed rock magnetic measurements (i.e., hysteresis loops, IRM acquisition curves, DC and AC demagnetization curves, ARM induction curves, FORCs, and low-temperature thermal demagnetization curves) on three sets of magnetosome-bearing samples with systematic variations in chain integrity and particle concentration. Magnetosomes were obtained from cultures of *Magnetospirillum magneticum* AMB-1. Our aim is to investigate the effects of chain dependent magnetic anisotropy and magnetostatic interactions on the bulk magnetic properties of magnetosomes. This is important for magnetofossil identification in natural samples.

2. Samples and Methods

2.1. Sample Preparation

[7] *M. magneticum* AMB-1 (ATCC strain 700264) has been cultured anaerobically at 26°C in 10 L of modified ATCC-recommended liquid medium with addition of 60 μM ferric quinate. Cells grown to the stationary phase were harvested by centrifugation. Three sets of samples with different degrees of magnetosome chain integrity were obtained by subjecting the whole cells to 3 ultrasonic treatments, i.e., in 30 ml of distilled water (set A1), NaOH (0.1 M) (set A2) and urea (8 M) (set A3) solutions. We used an ultrasonicator (VCX130, SONICS, USA) with 65 W power and 5 s pulse applied cycles followed by 5 s pauses for a total of 20 min for each treatment. Magnetosomes were collected with a bar magnet (5 mT max.) and washed five times with distilled water. Finally, each set of extracted magnetosomes was suspended in 3 mL of distilled water for subsequent dispersion experiments.

[8] Each set of extracted magnetosomes was equally divided into three groups (a, b and c). The (a) group (A1a to A3a) was directly frozen with liquid nitrogen and then freeze-dried without dilution. Groups (b) and (c) were dispersed by mixing with powdered calcium fluoride (CaF_2) to make samples with different degrees of particle concentration and interactions. The (b) group (A1b to A3b) was produced by dilution to ~0.15% (the similar dilution used by *Kopp et al.* [2006b]) in CaF_2 by mixing 1 mL of extracted-magnetosome suspension with 0.2 g CaF_2 powder, frozen with liquid nitrogen and freeze-dried. The (c) group (A1c to A3c) was prepared similar to group (b) but with a larger dilution factor by mixing with 1.0 g CaF_2 powder.

[9] To avoid post-oxidation of magnetosomes, the following strategies were adopted during sample preparation: (1) AMB-1 cells were harvested by centrifugation at 4°C and the whole-cell sample was freeze-dried; (2) ultrasonic disruption was carried out in an ice-bath (0°C) in an argon atmosphere; (3) magnetosome extraction, sample washing, and packing was undertaken inside an anaerobic chamber (Coy Labs, USA, $[O_2]$ <300 ppm). Distilled water, NaOH and urea solutions were pretreated by bubbling with nitrogen for 1 h to remove dissolved oxygen; and (4) all samples were maintained in pure nitrogen atmosphere at T = −20°C prior to magnetic measurements.

2.2. Room Temperature Magnetic Measurements

[10] Static IRM acquisition and DC demagnetization curves were measured up to 300 mT in 5 mT increments on previously demagnetized samples using a Model 3900 vibrating sample magnetometer (Princeton Measurements Corporation VSM3900, sensitivity = 0.5×10^{-9} Am^2). ARM acquisition, IRM and ARM AF demagnetization curves, as well as pulse-field IRM acquisition and demagnetization curves were measured with a 2G enterprises superconducting rock magnetometer system (2G-760) coupled with a Model 2G-660 automatic sample degaussing system (sensitivity = 2×10^{-12} Am^2). An ARM was acquired in an 80 mT AF with a DC bias field that was stepwise increased from 0 to 0.3 mT, followed by stepwise AF demagnetization up to 100 mT. Acquisition curves of pulse-field IRM were obtained in 5 mT increments with a pulse magnetizer, followed by stepwise demagnetization with a pulsed field in the opposition direction.

[11] To simplify comparison of remanence results, IRM acquisition curves were normalized to the SIRM for each sample, and backfield or reversed field demagnetization curves were rescaled as 1/2(1 + IRM($-H$)/SIRM). The median destructive field (MDF) corresponds to the pulsed field (MDF_{pf}) or AF (MDF_{af}) at which half of the SIRM or ARM is destroyed. To characterize magnetostatic interactions, the *R*-value of the Wohlfarth-Cisowski test

[*Cisowski*, 1981] was determined on the following pairs of acquisition and demagnetization curves: static-field IRM (R_{sf}) and pulse-field IRM (R_{pf}). The efficiency of weak-field ARM acquisition (ARM/SIRM versus DC bias field) was also used to estimate magnetostatic interactions [*Moskowitz et al.*, 1993; *Kobayashi et al.*, 2006; *Kopp et al.*, 2006b].

[12] Hysteresis loops were measured with the VSM between ±500 mT, and hysteresis parameters, including saturation magnetization (M_s), saturation remanence (M_{rs}), and coercivity (B_c) were determined after the high-field slope corrections fit to a linear or nonlinear functions [*Jackson and Solheid*, 2010]. Remanence coercivity (B_{cr}) was determined from DC demagnetization curves of SIRM. FORCs [*Pike et al.*, 1999; *Roberts et al.*, 2000] were measured according to the protocol described by *Egli et al.* [2010]. For each sample, 300 FORCs were measured with a positive saturation field of 500 mT and a field increment (δH) of 0.63 mT. FORC diagrams were calculated using the FORCinel version 1.21 software with a smoothing factor (SF) of 5 [*Harrison and Feinberg*, 2008]. According to the *Preisach* [1935] interpretation of the FORC diagram, the horizontal (B_c) and vertical (B_b) axes indicate the microcoercivity and interaction field distributions for SD particles, respectively [*Pike et al.*, 1999; *Roberts et al.*, 2000]. Two FORC parameters, median coercivity ($B_{c,FORC}$) and half-width interaction field ($B_{b,1/2}$), are defined as the median B_c which is given by the marginal coercivity distribution and as the interaction field value where the broadest B_b distribution reduces to half of its maximum, respectively [*Egli*, 2006b; *Egli et al.*, 2010; *Winklhofer and Zimanyi*, 2006].

2.3. Low-Temperature Magnetic Measurements

[13] Low-temperature magnetic measurements were performed with a Quantum Design Magnetic Property Measurement System (MPMS XP-5, sensitivity = 5.0×10^{-10} Am^2). ZFC and FC curves were obtained by cooling samples from 300 K to 10 K in zero field and in a 2.5-T field, respectively, followed by imparting a SIRM in a 2.5-T field (hereafter termed as $SIRM_{10K\_2.5T}$), and then measuring the remanence in zero field during warming to 300 K. The Verwey transition signature of magnetosome chains is characterized by the δ-ratio (δ_{FC}/δ_{ZFC}), in which δ_{FC} and δ_{ZFC} are calculated as $\delta = (M_{80K} - M_{150K})/M_{80K}$, where M_{80K} and M_{150K} are the remanences measured at 80 K and 150 K, respectively [*Moskowitz et al.*, 1993].

2.4. Electron Microscopy

[14] Intact cells or extracted magnetosomes of AMB-1 were deposited onto carbon-coated copper grids and studied by using a JEOL JEM-2010 transmission electron microscope (TEM) at a 200 kV accelerating voltage. For scanning electron microscope (SEM) observations, powder samples of extracted magnetosomes were mounted on an aluminum SEM stub using copper tape, and are then coated with gold (~5 nm in thickness). SEM analyses were performed on the Zeiss Supra 55 SEM microscope. The microscope was operated at 5 kV with a working distance of 7.5 mm. Two detectors were used: in-Lens detector for secondary electron imaging (nanotopography of the sample) and an Angle selective Backscattered (AsB) detector for low-angle backscattered electrons, which provide a contrast that is more sensitive to crystal orientation. The spatial arrangements of extracted magnetosomes and their dispersion states within CaF_2 matrix were examined in situ.

3. Results

3.1. Electron Microscopic Examinations

[15] TEM and SEM observations indicate that the sequential cell treatments for sample preparation produced an increasing degree of chain breakup and particle aggregation (Figure 1). The first-step treatment destroyed visible cell structures and caused some degree of chain aggregation (chain pairs), with most particles remaining in chains and associated with cell debris (Figures 1b and 1e). After the second-step treatment, magnetosome chains are still recognized, but are mostly packed to form large aggregates (Figure 1c). The third-step treatment led to magnetosome clumping (Figure 1d).

[16] SEM observations indicate that the CaF_2 particles have plate-like shapes with typical sizes of ~10 μm in plane length (Figure 1i). The extracted magnetosomes are attached to CaF_2 and are well dispersed in the diluted samples (Figures 1f–1j). Nevertheless, the main features of spatial arrangements of extracted magnetosomes still remain, i.e., isolated chains of magnetosomes occur predominantly in set A1 (e.g., Figures 1f, 1i, and 1j), short chains and individual particles coexist in set A2 (e.g., Figure 1g), and individual particles dominate set A3 (e.g., Figure 1h).

3.2. FORC Diagrams

[17] Coercivity and interaction distribution trends can be recognized in the FORC diagrams in Figure 2.

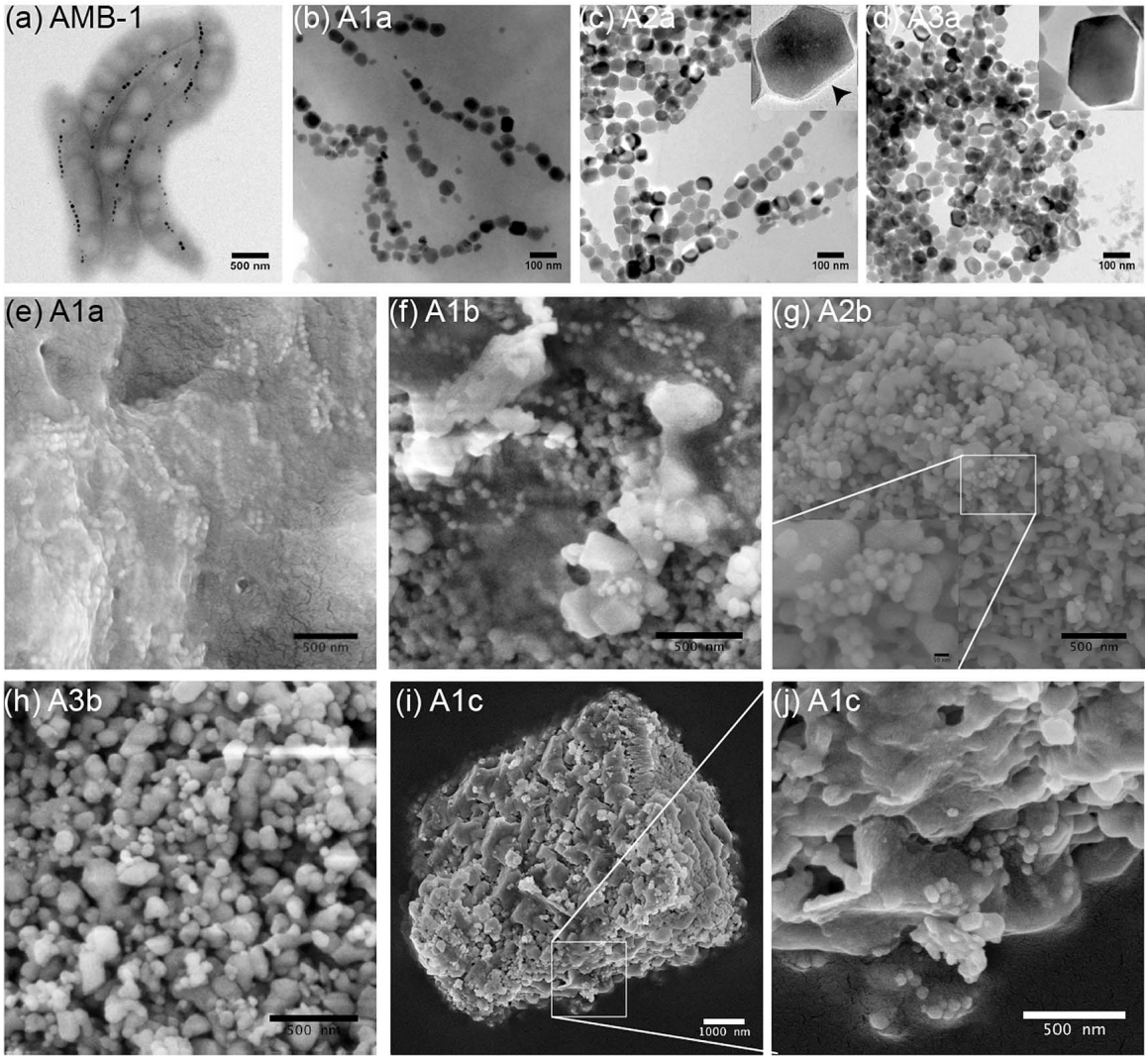

Figure 1. Electron microscopic observations of *M. magneticum* AMB-1 magnetosomes. (a) Typical TEM image of intact AMB-1 cells. TEM images of extracted magnetosomes (without dilution) after (b) one, (c) two, and (d) three steps of the disaggregation treatment. The upper right-hand insets in Figures 1c and 1d are of a single particle with (arrow) and without (no arrow) magnetosome membranes, respectively. Typical SEM images of extracted magnetosomes after (e) one step of treatment, and (f–j) CaF_2-diluted samples of extracted magnetosomes. Note: extracted magnetosomes within organic or/and CaF_2 matrix can be recognized based on their typical chain structures and grain size of ~50 nm, as well as their contrast from the matrix.

The whole-cell sample has a FORC distribution with a clear so-called central ridge feature [*Egli et al.*, 2010], which indicates no or negligible inter-cell or inter-chain interactions [*Pike et al.*, 1999; *Roberts et al.*, 2000]. The FORC diagram for sample A1a has a typical "tear drop" shape of interacting SD particles, as described by *Pike et al.* [1999] and *Egli* [2006b]. FORC diagrams for samples A2a and A3a (also without dilution) exhibit strong magnetostatic interactions between individual particles, in which the contours intersect the B_b axis and significantly expand in the vertical direction (Table 1). As expected, dilution produces FORC diagrams with a smaller vertical spread, and thus a less amount of magnetostatic interactions. Overall, the vertical spread of FORC diagram increases with increasing particle concentration (from right to left in Figure 2), and with increasingly strong ultrasonic treatment (from top to bottom). The central ridge of FORC diagram, which is characteristic of non-interacting and weakly interacting uniaxial SD particles [*Egli et al.*, 2010], becomes sharper with dilution (from left to right) and with decreasingly ultrasonic treatment (from bottom to top). The position of the peak of the FORC distribution is not significantly affected by dilution, but

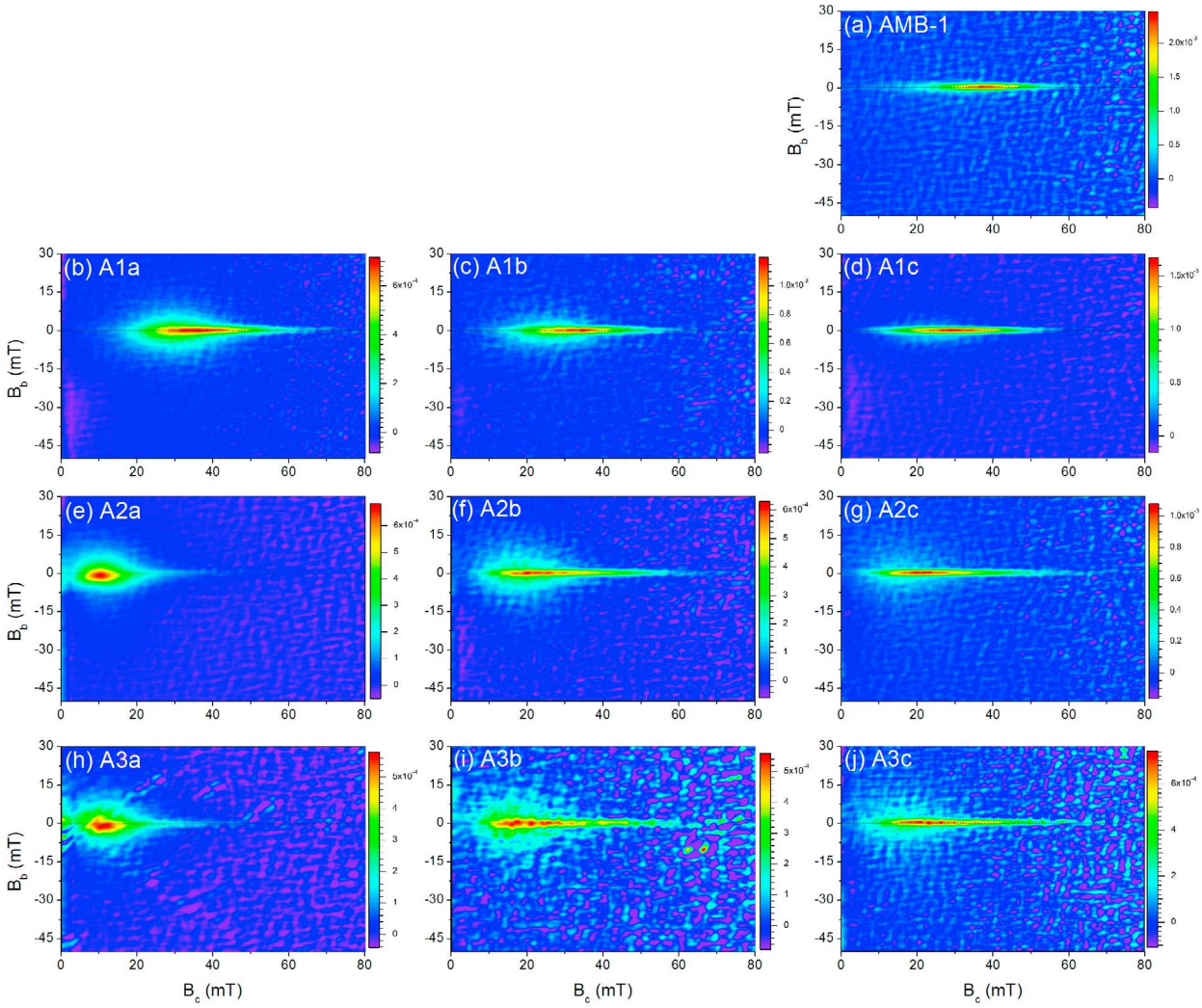

Figure 2. FORC diagrams measured on the studied series of AMB-1 magnetosome samples using δH = 0.63 mT, SF = 5, and ΔH = 3.5 mT [*Harrison and Feinberg*, 2008; *Egli et al.*, 2010]. The FORC diagrams indicate SD assemblages of AMB-1 magnetosomes with different magnetostatic interactions and magnetic anisotropy. The vertical spread of FORC diagram increases with increasing particle concentration (from right to left), and with increasingly strong ultrasonic treatment (from top to bottom). The central ridge of FORC diagram, which is characteristic of non-interacting and weakly interacting uniaxial SD particles [*Egli et al.*, 2010], becomes sharper with dilution (from left to right), and with decreasingly ultrasonic treatment (from bottom to top). The position of the peak of the FORC distribution is not significantly affected by dilution, but shifts to lower B_c values with increasingly strong treatment.

shifts to lower B_c values with increasingly strong treatment (Table 1).

3.3. ARM/SIRM

[18] ARM acquisition curves normalized by SIRM are shown in Figure 3. As expected, ARM is lowered by increasing magnetostatic interactions from chain aggregates to disordered magnetosome clumps (i.e., AMB > A1a > A2a > A3a). Progressive sample dilution also decreases magnetostatic interactions (e.g., A1a < A1b < A1c). ARM acquisition curves for the extracted magnetosome samples are intermediate between the limiting cases of non-interacting SD particles and chains (e.g., AMB-1 cells) and highly interacting SD particles from Chiton teeth [*Cisowski*, 1981], respectively.

3.4. Remanent Magnetization Curves

[19] Results of the Wohlfarth-Cisowski test [*Cisowski*, 1981], where the shape of acquisition

Table 1. Room Temperature Magnetic Parameters for the Studied Series of AMB-1 Magnetosome Samples[a]

	Remanent Coercivity Spectra					Hysteresis Loop				FORC	
Sample	R_{sf}	R_{pf}	MDF_{pf} (mT)	MDF_{af} (mT)	χ_{ARM}/SIRM ($\times 10^{-3}$ m/A) ($B_{applied}$=0.1 mT)	B_c (mT)	B_{cr} (mT)	B_{cr}/B_c	M_{rs}/M_s	$B_{c,FORC}$ (mT)	$B_{b,1/2}$ (B_c)[b] (mT)
AMB	0.48	0.49	48.2	42.9	1.38	30.5	37.4	1.23	0.50	36.7	1.2 (37)
A1a	0.43	0.43	34.3	31.3	0.35	25.2	33.8	1.34	0.43	33.2	3.5 (22)
A1b	0.45	0.45	33.1	33.4	0.73	23.2	31.2	1.34	0.43	30.1	2.2 (20)
A1c	0.46	0.46	32.4	36.2	1.19	21.3	29.6	1.39	0.44	28.5	1.4 (20)
A2a	0.41	0.40	18.6	17.0	0.25	9.2	15.1	1.64	0.24	12.7	5.1 (5)
A2b	0.43	0.44	26.2	28.0	0.55	15.8	25.1	1.59	0.32	22.1	2.1 (14)
A2c	0.44	0.45	26.5	30.4	0.90	15.0	23.6	1.57	0.33	21.9	1.5 (14)
A3a	0.40	0.38	18.2	15.8	0.23	7.9	14.7	1.86	0.22	12.8	6.9 (5)
A3b	0.42	0.43	23.0	28.2	0.52	15.4	24.4	1.58	0.32	20.5	3.3 (15)
A3c	0.43	0.44	27.7	30.8	0.65	15.3	24.4	1.59	0.32	21.8	1.7 (16)

[a]Notation: R, from the Wohlfarth-Cisowski test, is determined by the following pairs of acquisition and demagnetization curves: DC field IRM (R_{sf}) and pulsed-field IRM (R_{pf}); MDF, median destructive field, corresponds to the pulsed-field (MDF_{pf}) or alternating field (MDF_{af}), at which half of a total remanence is destroyed; χ_{ARM}/SIRM ($B_{applied}$=0.1 mT), χ_{ARM} (χ_{ARM}=$ARM_{0.1\ mT}$/79.5775 A/m) normalized to SIRM; B_{cr}, coercivity of remanence, is determined by DC demagnetization curve of SIRM; B_c, M_{rs} and M_s indicate coercivity, remanent magnetization and saturation magnetization, respectively, which are determined from room temperature hysteresis loops; $B_{c,FORC}$ and $B_{b,1/2}$ are defined as the median coercivity of the marginal coercivity distribution and as the interaction field value where the broadest B_b distribution reduces to half of its maximum, respectively.

[b]The B_c in parentheses indicates the coercivity value where the broadest B_b distribution is obtained.

and demagnetization curves, normalized to SIRM, are compared and shown in Figure 4. In an ideal case of non-interacting SD particles, the IRM acquisition and demagnetization curves are symmetric with respect to each other and cross at R = 0.5. Crossing values R <0.5 are indicative of magnetostatic interactions in SD particles or of non-SD behavior [e.g., *Moskowitz et al.*, 1988, 1993]. In the case of the present study, this consideration is irrelevant because all of the particles under investigation are SD. The R-parameters for the whole-cell sample AMB-1 are close to 0.5 (e.g., R_{sf} = 0.48 and R_{pf} = 0.49; Figure 4a and Table 1), which confirms that isolated magnetosome chains behave like non-interacting SD particles, as also shown by FORC measurements. Magnetization curves for AMB-1 are symmetric, with no low- or high-coercivity tails: this is typical of MTB magnetite due to the narrow distribution of anisotropies and grain sizes [e.g., *Moskowitz et al.*, 1993].

[20] Magnetization curves for samples with a decreasing degree of chain integrity (i.e., AMB > A1a > A2a > A3a) have progressively decreasing R and MDF values (Table 1); the magnetization curves also become progressively more right-skewed with decreasing chain integrity (Figures 4b–4d). In contrast, sample dilution tends to increase R toward the value typical of intact cells (e.g., A1a < A1b < A1c) (Table 1). For sample sets A2 and A3, MDF, B_{cr} and B_c values increase with increasing dilution, while they slightly decrease for set A1 (Table 1). A possible interpretation is that magnetosome chains were fragmented during dilution, resulting in a slightly decreased anisotropy.

3.5. Hysteresis Parameters

[21] On a Day plot (B_{cr}/B_c versus M_{rs}/M_s) [*Day et al.*, 1977; *Dunlop*, 2002], data for the whole-cell sample of AMB-1 fall in the same cluster as for intact MTB cells [*Moskowitz et al.*, 1993; *Pan et al.*, 2005b; *Lin and Pan*, 2009; *Zhu et al.*, 2010], with B_{cr}/B_c and M_{rs}/M_s values typical of non-interacting, uniaxial SD particles [*Cisowski*, 1981]. With progressive chain disruption but no dilution, the hysteresis parameters move away from the uniaxial SD region along the SD-MD mixing line (Figure 5 and Table 1). Hysteresis parameters for set A1 (black circles) seem to be less affected by dilution and are close to the uniaxial SD region. Sets A2 and A3 have lower M_{rs}/M_s and higher B_{cr}/B_c values. Dilution treatments result in the diluted A2 and A3 samples moving back slightly toward the uniaxial SD region (Figure 5).

3.6. ZFC and FC SIRM Curves

[22] Thermal demagnetization curves of $SIRM_{10K\_2.5T}$ for all nine extracted magnetosome samples and the whole-cell sample are shown in Figure 6. Compared with their intact counterpart (AMB-1), both ZFC and FC warming curves have steep SIRM decay for the extracted magnetosomes. The value of $TD_{10\rightarrow30K}$, which is equal to 100 × $(M_{10K} - M_{30K})/M_{10K}$, increases with progressive

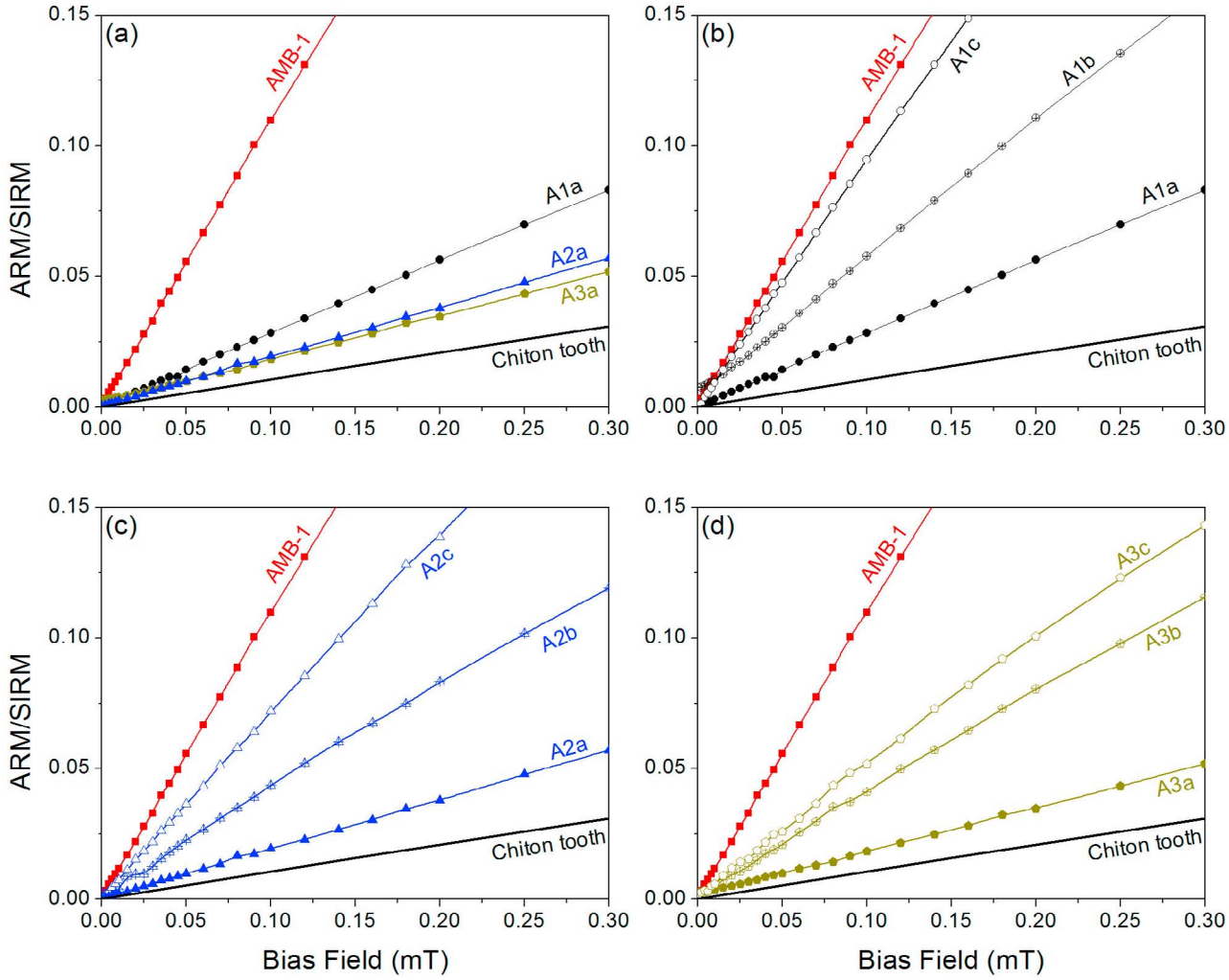

Figure 3. Normalized ARM as a function of applied DC field for the studied series of AMB-1 magnetosome samples. ARM is normalized by SIRM. Data for Chiton SD magnetite are from *Cisowski* [1981].

cell disruption (e.g., AMB <A1a < A2a < A3a), and decreases with progressive sample dilution (e.g., A2a > A2b > A2c) with the exception for the A1 set (Table 2). The remanence loss between 10 and 30 K can be attributed to the combined effects of magnetostatic interactions and superparamagnetic (SPM) relaxation [*Pike et al.*, 2000]. The latter might emerge in collapsed chains because of the decrease of uniaxial anisotropy.

[23] All samples have the same Verwey transition temperature of 102 ± 2 K, which is much lower than that of stoichiometric magnetite [*Walz*, 2002], but comparable to that of fresh AMB-1 cell samples (104 K) and other MTB strains that have not undergone further oxidation beyond the possibly original non-stoichiometric state [*Moskowitz et al.*, 2008; *Li et al.*, 2009; *Li and Pan*, 2012]. Compared with the whole-cell sample AMB-1, extracted magnetosome samples have much higher δ_{ZFC} but lower δ-ratio values (Table 2). Eight extracted magnetosome samples with the exception of A1c have δ-ratios between 1.20 and 1.86, which is lower than 2.0, and thus fail the Moskowitz test as expected [*Moskowitz et al.*, 1993; *Weiss et al.*, 2004a; *Li et al.*, 2010a]. The A1 sample set, which consists of intact chains with various dilutions, is characterized by relatively higher δ-ratios and lower δ_{ZFC} values compared with A2 and A3 sets. Within the same sample set, dilution increases the δ-ratios but reduces δ_{ZFC} values (Table 2).

4. Discussion

4.1. Characterizing Magnetostatic Interactions

[24] χ_{ARM}/SIRM ratios for samples from this study are plotted versus corresponding $B_{b,1/2}$ and R_{sf}

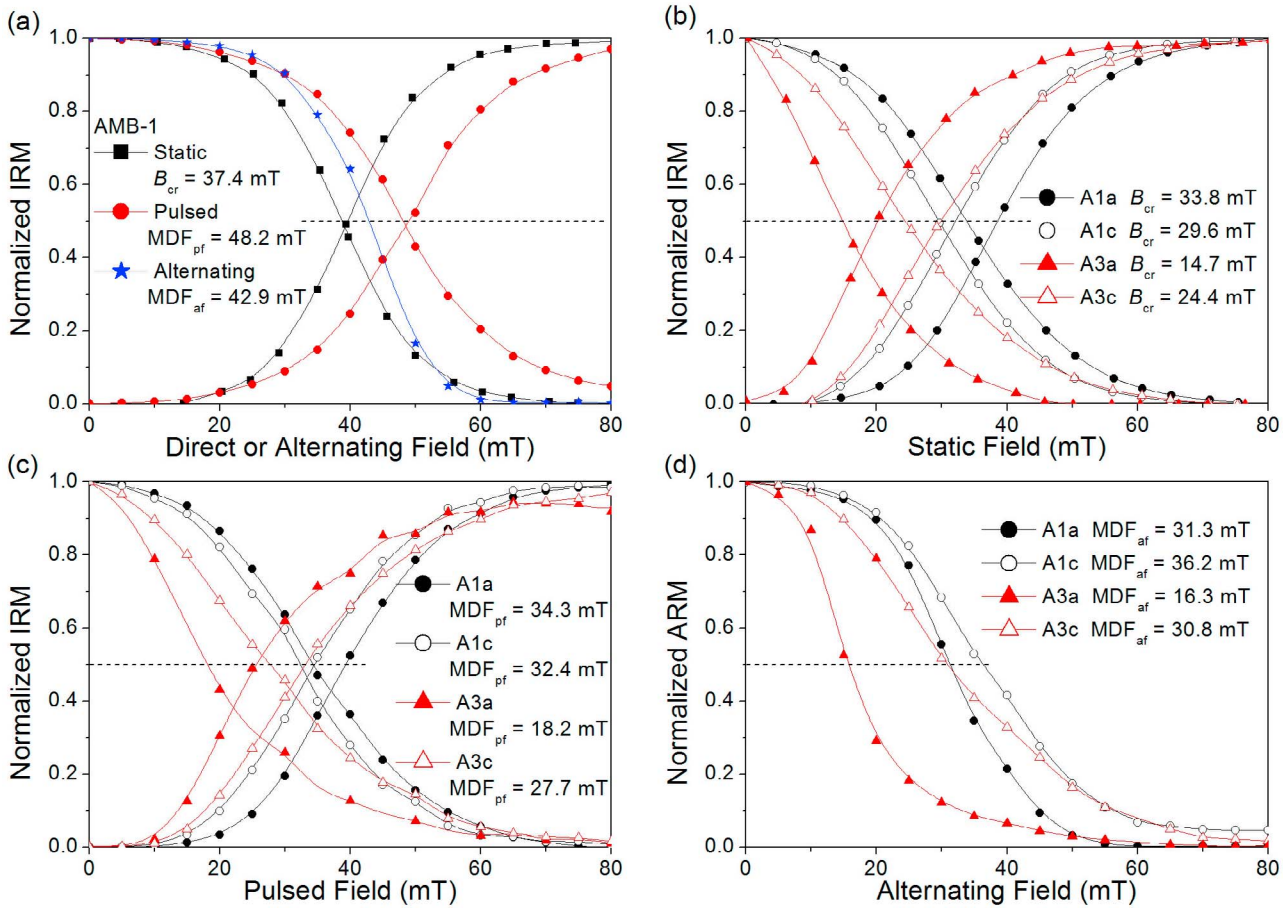

Figure 4. Normalized IRM acquisition and demagnetization curves, and ARM AF demagnetization curves for (a) whole-cell sample (AMB-1), and (b-d) extracted magnetosome samples. In Figure 4a, results are shown for static, pulsed and AF demagnetization for AMB-1, while results are shown for extracted magnetosomes in Figures 4b–4d, with static field acquisition and demagnetization (Figure 4b), pulsed field acquisition and demagnetization (Figure 4c), and AF demagnetization (Figure 4d).

values in Figure 7. χ_{ARM}/SIRM correlates well with $B_{b,1/2}$ and R_{sf}, which indicates their consistency for characterizing magnetostatic interactions. Existing models of interaction effects on ARM [*Egli*, 2006a] and FORC measurements [*Egli*, 2006b] predict the χ_{ARM}/SIRM and the vertical half-width of the FORC distribution for interacting SD particles as a function of their volume concentration (i.e., the volume fraction p of the sample that is occupied by the particles). Comparison of these parameters for the same concentration values defines a black line in Figure 7a (data courtesy of Ramon Egli). Using the initial χ_{ARM}/SIRM of AMB-1 reported in Table 1 as the non-interacting value (i.e., r_a in *Egli* [2006a]), the resulting curve is consistent with our experimental data. The weakly interacting samples (i.e., A1b, A2b, A3b, A2c and A3c), i.e., those where the coercivity is larger than the interaction field, are in good agreement with the theoretical correlation of *Egli* [2006a, 2006b] between these parameters. Data for high interacting samples (i.e., A1a, A2a and A3a) and non-interacting samples (i.e., AMB-1 and A1c) agree less well with the theoretical curve. The data below the theoretical curve for samples of A1a, A2a and A3a can be interpreted as their more or less bimodal FORC diagrams (Figures 2b, 2e, and 2h), which may result from a non-homogeneous assemblage of interacting particles or/and a mixture of interacting particles and more or less weakly or non-interacting particles (e.g., residual magnetosome chains) [*Chen et al.*, 2007]. For non-interacting sample, the lower limit of the vertical width of the FORC diagram is set by the resolution of the measurements ΔH ($\delta H \times$ (SF + 1/2) [*Egli et al.*, 2010]. It ought to have zero vertical width if it is perfectly defined (i.e., $\Delta H = 0$). However, it will always have a nonzero value of $B_{b,1/2}$ because of the finiteness of the field steps used in FORC measurements and the smoothing factor used

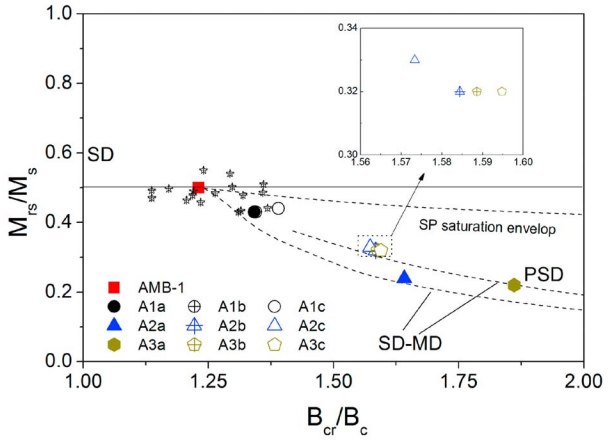

Figure 5. Day plot (B_{cr}/B_c versus M_{rs}/M_s) for the studied series of AMB-1 magnetosome samples. Stars with crosses indicate whole-cell samples of MTB reported in previous studies [*Moskowitz et al.*, 1993; *Pan et al.*, 2005b; *Lin and Pan*, 2009; *Zhu et al.*, 2010]. The dashed lines are mixing lines for SD-MD and SD-SP mixtures from *Dunlop* [2002].

when processing FORC data [*Egli et al.*, 2010]. The data above the theoretical curve for AMB-1 and A1c are related to an experimental limitation of FORC measurements in this study, e.g., $\Delta H = 3.5$ mT.

[25] ARM has been widely used for characterizing and identifying magnetic particles in geological samples, e.g., as a grain size indicator in rock magnetism [*Johnson et al.*, 1975; *King et al.*, 1982], and as a normalization factor in paleointensity studies [*Banerjee and Mellema*, 1974; *Shaw*, 1974; *Yu*, 2010], as well as to quantify magnetofossils in fresh and marine sediments [*Petersen et al.*, 1986; *Egli*, 2004c; *Paasche and Løvlie*, 2011]. However, magnetostatic interactions reduce the χ_{ARM}/SIRM and ARM/SIRM ratios of interacting SD particles to an extent that depends on their volume concentration, as observed experimentally [*Sugiura*, 1979], and predicted by analytical models [*Egli*, 2006a]. Experimental data from this study indicate that ARM is strongly affected by and highly sensitive to magnetostatic interactions (Figure 3). Even a slight increase in the vertical spread of the FORC distribution or a slight decrease of the crossover parameter R used for the Wohlfarth-Cisowski test is associated with a strong decrease in ARM/SIRM. For example, compared with the initial χ_{ARM}/SIRM value of the whole-cell AMB-1 sample, which is indicative of non-interacting value, ARM for A1b is reduced to ~50% while accompanied by a small change in $B_{b,1/2}$ (e.g., 1.2 mT and 2.2 mT for AMB-1 and A1b, respectively) and R (e.g., 0.49 and 0.45 for AMB-1 and A1b, respectively) (Table 1). Most importantly, experimental data from this study also demonstrate that χ_{ARM}/SIRM does not decrease below a critical threshold of 1×10^{-3} m/A if magnetosome chains remain intact and well dispersed (i.e., whole-cell sample AMB-1 and extracted-magnetosome sample A1c). On the other hand, caution should be used when screening geological samples for magnetofossils using ARM measurements, because chain collapse can lower the χ_{ARM}/SIRM ratio below this threshold, which is often considered diagnostic of the presence of magnetofossils [*Moskowitz et al.*, 1993].

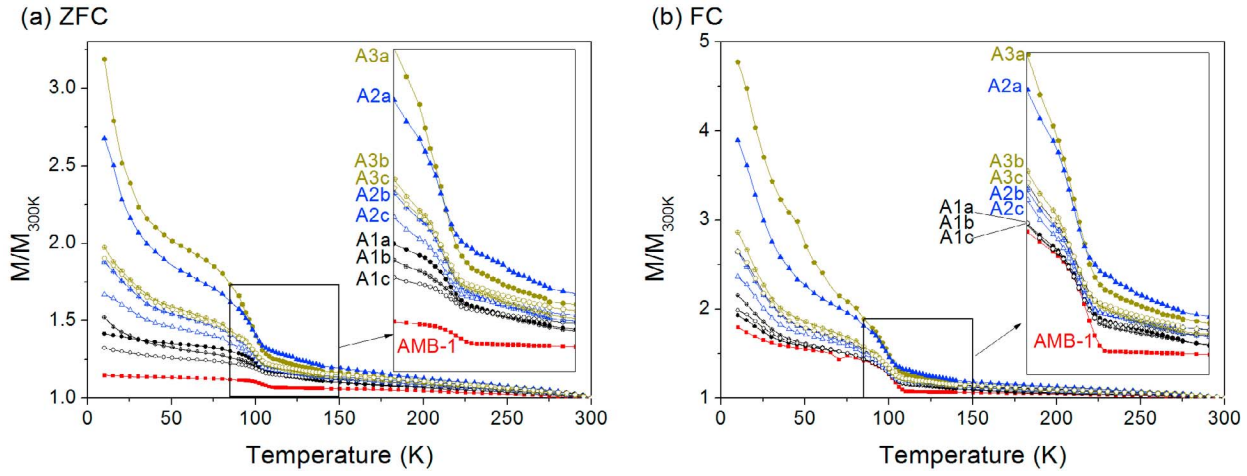

Figure 6. Zero-field thermal demagnetization of SIRM produced in a 2.5-T field at 10 K for the studied series of AMB-1 magnetosome samples. (a) ZFC warming curves. (b) FC warming curves. The data are normalized to their own remanences at 300 K.

Table 2. Low-Temperature Magnetic Parameters for the Studied Series of AMB-1 Magnetosome Samples[a]

					FC-TD (%)		ZFC-TD (%)	
Sample	T_v (K)	δ_{FC}	δ_{ZFC}	δ_{FC}/δ_{ZFC}	10 → 30 K	10 → 300 K	10 → 30 K	10 → 300 K
AMB	104	0.27	0.056	4.81	9.8	44.2	0.8	12.9
A1a	100	0.26	0.16	1.62	12.6	48.1	2.7	29.3
A1b	102	0.26	0.14	1.86	17.7	53.6	9.5	34.3
A1c	102	0.24	0.092	2.61	13.3	49.6	3.0	24.4
A2a	100	0.38	0.29	1.31	29.2	74.4	22.7	62.7
A2b	100	0.29	0.22	1.34	23.1	62.2	11.9	46.8
A2c	100	0.26	0.18	1.50	19.3	57.6	8.3	40.2
A3a	100	0.42	0.35	1.20	28.1	79.1	30.0	68.7
A3b	100	0.31	0.23	1.34	26.1	65.1	13.3	49.4
A3c	102	0.29	0.21	1.39	22.4	62.2	11.1	47.4

[a]Notation: T_v, Verwey transition temperature, is determined from the maximum of the dM/dT of FC data; δ_{FC} and δ_{ZFC} is calculated from $\delta=(M_{80K}-M_{150K})/M_{80K}$ (M_{80K} and M_{150K} are the remanences measured at 80 K and 150 K, respectively). TD%(X→Y K)=$(M_X-M_Y)/M_X\times100$ (M_X and M_Y are the remanences measured at X K and Y K, respectively).

4.2. Mechanism of $B_{c,FORC}$

[26] The FORC technique has advantages in simultaneously visualizing the microcoercivity and interaction field distributions, as well as domain states of magnetic minerals in measured samples [*Pike et al.*, 1999; *Roberts et al.*, 2000], and thus has been used to characterize magnetosome biomineralization [*Carvallo et al.*, 2009; *Li et al.*, 2009] and quantitatively detect magnetofossils [*Chen et al.*, 2007; *Egli et al.*, 2010; *Roberts et al.*, 2011, 2012]. Models for the FORC signature of SD particles have shown that B_c in the FORC diagram corresponds to the switching field, whose median is the coercivity of remanence B_{cr} [*Egli*, 2006b; *Egli et al.*, 2010; *Winklhofer and Zimanyi*, 2006]. To examine this idea, $B_{c,FORC}$ values for samples in this study are plotted versus their corresponding B_c, B_{cr}, MDF_{pf} and MDF_{af} values in Figure 8.

[27] $B_{c,FORC}$ has good linear correlation with B_c and B_{cr}, and poorer linear correlation with MDF_{pf} and MDF_{af}. Furthermore, for the measured samples, B_c is systematically lower than the corresponding $B_{c,FORC}$ values, while B_{cr} values nicely fall onto the s = 1 line with $B_{c,FORC}$ values. FORC and hysteresis

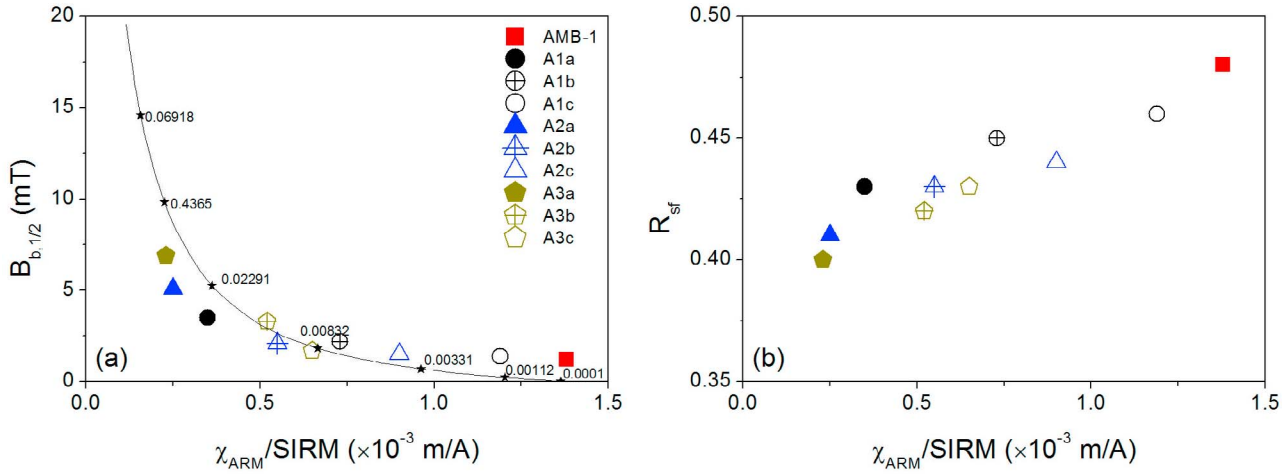

Figure 7. Correlation between χ_{ARM}/SIRM and the half width of the interaction field distribution from the FORC diagram ($B_{b,1/2}$), the Wohlfarth-Cisowski test (R_{sf}) for characterizing magnetostatic interactions in the studied series of AMB-1 magnetosome samples. (a) χ_{ARM}/SIRM (at $B_{applied}$ = 0.1 mT) versus $B_{b,1/2}$. The black line is a theoretically simulated relationship between χ_{ARM}/SIRM and $B_{b,1/2}$ for interacting SD particles as a function of their volume concentration, and the number indicates packing fraction value p (data courtesy of Ramon Egli) [*Egli*, 2006a, 2006b]. (b) χ_{ARM}/SIRM versus R_{sf}. χ_{ARM}/SIRM is determined from ARM acquisition, where χ_{ARM} = ARM_b/b, where b is the bias field in A/m (here b = 0.1 mT = 79.5775 A/m for magnetite). $B_{b,1/2}$ and R_{sf} are determined from the FORC distribution and normalized IRM acquisition and demagnetization curves, respectively.

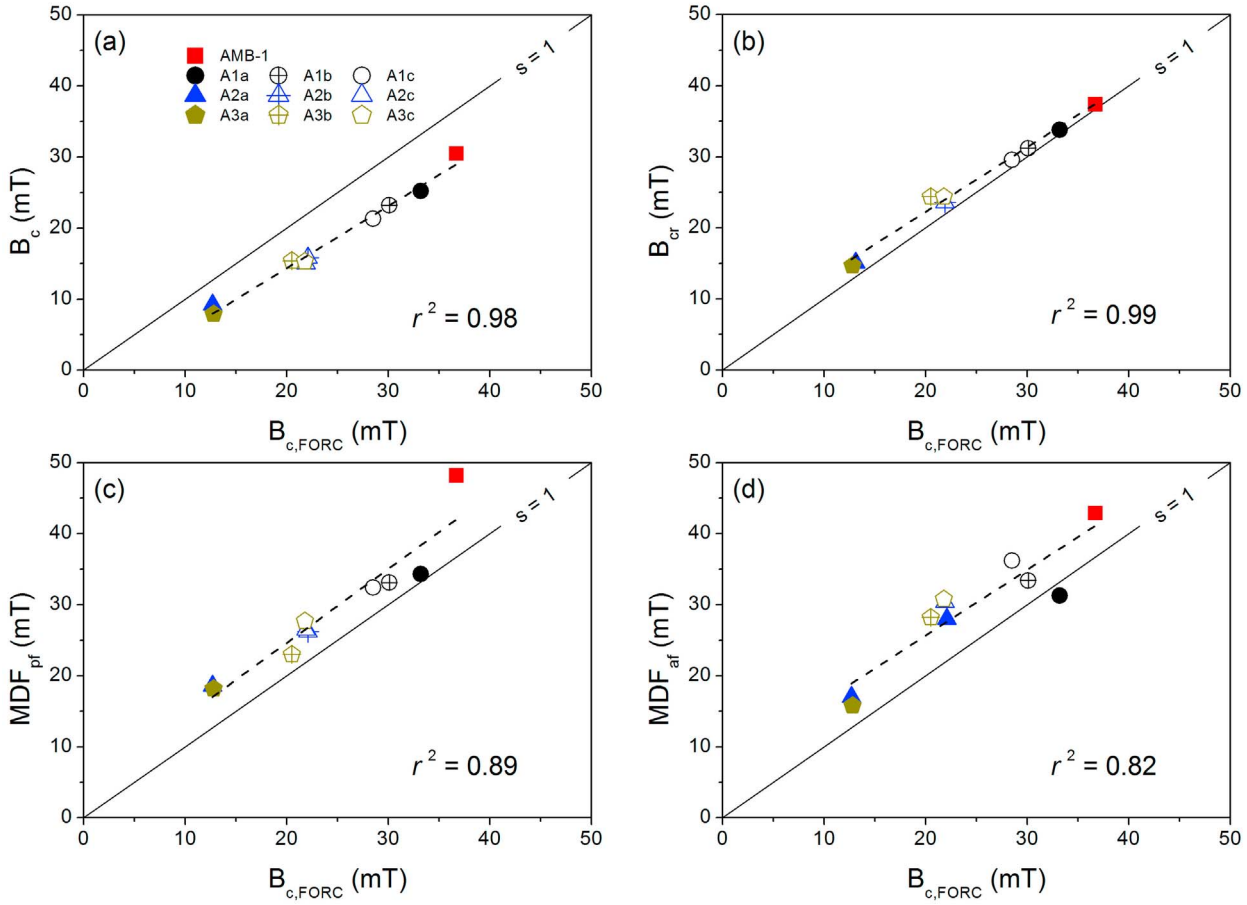

Figure 8. Correlation between coercivity (B_c), remanence coercivity (B_{cr}), median destructive field (MDF) and $B_{c,FORC}$ for the studied series of AMB-1 magnetosome samples. B_c, B_{cr}, MDF_{pf}, MDF_{af}, and $B_{c,FORC}$ are determined from hysteresis loops, DC demagnetization curves for SIRM, reversed pulsed-field demagnetization of SIRM, AF demagnetization of ARM, and FORC distributions, respectively. The dashed lines are regression fits to the measured data.

loop measurements on oriented samples of uncultured MYR-1 [*Li et al.*, 2010b] at various angles with respect to the magnetosome chain direction indicate a strong linear correlation between $B_{c,FORC}$ and B_{cr}, but poor correlation between $B_{c,FORC}$ and B_c. Taken together, these studies reinforce the idea that $B_{c,FORC}$ is equivalent to B_{cr} rather than B_c.

4.3. The δ-Plot and Identification of Magnetofossils

[28] Experiments in this study indicate that both intact cells of AMB-1 and extracted magnetosomes in well-dispersed chains have δ-ratios larger than the threshold of 2.0, which supports the validity of the Moskowitz test [*Moskowitz et al.*, 1993] for magnetofossil identification. In contrast, increasing degrees of chain disruption or particle aggregation, or both, produce lower δ-ratios and higher δ_{ZFC} values, which makes the Verwey transition signature more similar to that of abiogenic assemblages of SD magnetic particles [*Moskowitz et al.*, 1993; *Carter-Stiglitz et al.*, 2002; *Li et al.*, 2010a]. This trend is summarized in a plot of δ_{ZFC} versus δ_{FC}/δ_{ZFC} (hereafter referred to as the δ-plot), where these data can be fitted by the function $\delta_{FC}/\delta_{ZFC} = 7.11\ \exp(-\delta_{ZFC}/0.057) + 6583.22\exp(-\delta_{ZFC}/0.0063) + 1.21$ ($r^2 = 0.999$) (Figure 9).

[29] Several studies have demonstrated that the test of *Moskowitz et al.* [1993] for identifying magnetofossils is regularly compromised by low-temperature oxidation of magnetosomes or/and by physical disruption of magnetosome chains [*Moskowitz et al.*, 1993; *Smirnov and Tarduno*, 2000; *Passier and Dekkers*, 2002; *Weiss et al.*, 2004a; *Pan et al.*, 2005a; *Housen and Moskowitz*, 2006; *Roberts et al.*, 2012]. Given that oxidation can largely be precluded in the present study of fresh material, the present results provide an opportunity to assess how

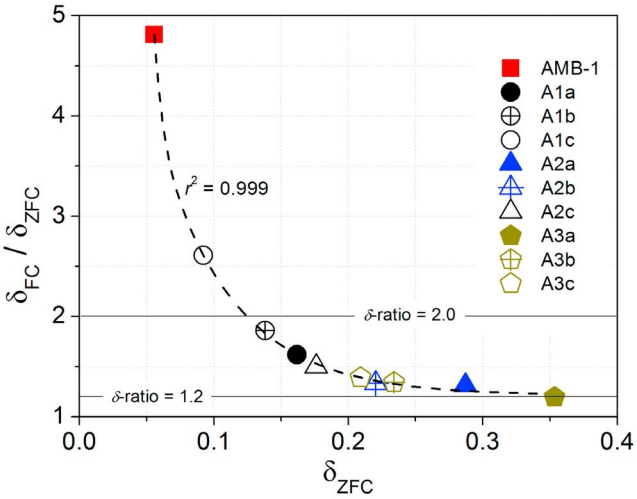

Figure 9. δ-plots (δ_{ZFC} versus δ_{FC}/δ_{ZFC}) for the studied series of AMB-1 magnetosome samples. The black dashed line is a regression fit to the measured data.

magnetosome chain disruption affects the δ-ratio. The δ-plot nicely reflects the spatial and geometric arrangement of magnetosome chains and can therefore be used to identify unoxidized magnetofossils in natural samples. It has been shown that the FMR fingerprints of magnetosome chains are unique and seem to be less susceptible to particle oxidation [*Weiss et al.*, 2004a; *Kopp et al.*, 2006a; *Kopp and Kirschvink*, 2008; *Chang et al.*, 2012], and therefore useful in identifying magnetofossils in geological samples [*Kopp et al.*, 2006a, 2007, 2009; *Gehring et al.*, 2011; *Kind et al.*, 2011; *Roberts et al.*, 2011, 2012]. Moreover, the sharp crystal morphology and grain size distribution of magnetosomes (magnetofossils) is also useful for detecting magnetofossils [*Arató et al.*, 2005]. Therefore, combined macro-micro approaches, i.e., rock magnetism, FMR and TEM, are the safest ways to unambiguously identify and quantify magnetofossils preserved in natural samples.

5. Conclusions

[30] Detailed rock magnetic analyses of cultured MTB (i.e., AMB-1) that were subjected to a varying physical and chemical treatments that produce increasing cell and magnetosome disruption were made to assess changes in the magnetic signature of magnetosomes associated with chain disruption. With progressive chain breakup or/and particle clumping, the magnetic parameters B_c, B_{cr}, MDF, $B_{c,FORC}$, χ_{ARM}/SIRM and δ-ratio decrease, while $B_{b,1/2}$ and δ_{ZFC} values increase. This indicates that rock magnetic measurements are sensitive to both magnetic anisotropy and magnetostatic interactions, which are useful for qualitatively and quantitatively detecting magnetofossils in geological samples. For samples with predominantly SD magnetic particles and relatively narrow grain size distributions (e.g., MTB magnetite), the χ_{ARM}/SIRM or ARM/SIRM ratios appear to be more sensitive to the degree of magnetostatic interactions. By comparison, results from this study reinforce the idea that $B_{c,FORC}$ is equivalent to B_{cr} rather than B_c. The δ-plot (δ_{ZFC} versus δ_{FC}/δ_{ZFC}), which summarizes Verwey transition properties, correlates well with the spatial and geometric arrangements of magnetosomes, and could provide a new method to diagnose unoxidized magnetofossils. We propose that comprehensive analyses (e.g., χ_{ARM}/SIRM, FORC, δ-plot, FMR and TEM) are needed to effectively detect magnetofossils in bulk natural samples.

Acknowledgments

[31] This work was supported by the CAS/SAFEA International Partnership Program for Creative Research Teams (KZCX2-YW-T10) and NSFC grants (41004024, 410250113, and 40974036). J.H.L. is grateful for support from the China Postdoctoral Science Foundation (CPSC grant 201104144). Y.X.P. and Q.S.L. acknowledge support from the CAS '100' Talents Program. We are grateful to Ramon Egli and Andrew P. Roberts, and other two anonymous reviewers for their constructive comments that significantly improved the original manuscript. We thank Richard J. Harrison for useful discussions concerning FORC data processing. We also thank Haitao Chen for kind assistance with FORC re-measurements. TEM observations were performed at the Technical Institute of Physics and Chemistry, Chinese Academy of Sciences (Beijing). SEM observations were performed at the Institut de Minéralogie et de Physique des Milieux Condensés (IMPMC, CNRS-UPMC, Paris).

References

Arató, B., Z. Szanyi, C. Flies, D. Schüler, R. B. Frankel, P. R. Buseck, and M. Pósfai (2005), Crystal-size and shape distributions of magnetite from uncultured magnetotactic bacteria as a potential biomarker, *Am. Mineral.*, *90*, 1233–1240, doi:10.2138/am.2005.1778.

Banerjee, S. K., and J. P. Mellema (1974), A new method for the determination of paleointensity from the A.R.M. properties of rocks, *Earth Planet. Sci. Lett.*, *23*, 177–184, doi:10.1016/0012-821X(74)90190-3.

Bazylinski, D. A., and R. B. Frankel (2004), Magnetosome formation in prokaryotes, *Nat. Rev. Microbiol.*, *2*, 217–230, doi:10.1038/nrmicro842.

Bazylinski, D. A., A. J. Dean, T. J. Williams, L. K. Long, S. L. Middleton, and B. L. Dubbels (2004), Chemolithoautotrophy in the marine, magnetotactic bacterial strains MV-1 and MV-2, *Arch. Microbiol.*, *182*, 373–387, doi:10.1007/s00203-004-0716-y.

Carter-Stiglitz, B., M. Jackson, and B. M. Moskowitz (2002), Low-temperature remanence in stable single domain magnetite, *Geophys. Res. Lett.*, *29*(7), 1129, doi:10.1029/2001GL014197.

Carvallo, C., S. Hickey, D. Faivre, and N. Menguy (2009), Formation of magnetite in *Magnetospirillum gryphiswaldense* studied with FORC diagrams, *Earth Planets Space*, *61*, 143–150.

Chang, L., M. Winklhofer, A. P. Roberts, M. J. Dekkers, C.-S. Horng, L. Hu, and Q. Chen (2012), Ferromagnetic resonance characterization of greigite (Fe_3S_4), monoclinic pyrrhotite (Fe_7S_8), and non-interacting titanomagnetite ($Fe_{3-x}Ti_xO_4$), *Geochem. Geophys. Geosyst.*, *13*, Q05Z41, doi:10.1029/2012GC004063.

Chang, S. B. R., and J. L. Kirschvink (1989), Magnetofossils, the magnetization of sediments, and the evolution of magnetite biomineralization, *Annu. Rev. Earth Planet. Sci.*, *17*, 169–195, doi:10.1146/annurev.ea.17.050189.001125.

Chen, A. P., R. Egli, and B. M. Moskowitz (2007), First-order reversal curve (FORC) diagrams of natural and cultured biogenic magnetic particles, *J. Geophys. Res.*, *112*, B08S90, doi:10.1029/2006JB004575.

Cisowski, S. (1981), Interacting vs. non-interacting single domain behavior in natural and synthetic samples, *Phys. Earth Planet. Inter.*, *26*, 56–62, doi:10.1016/0031-9201(81)90097-2.

Day, R., M. Fuller, and V. A. Schmidt (1977), Hysteresis properties of titanomagnetites: Grain size and composition dependence, *Phys. Earth Planet. Inter.*, *13*, 260–267, doi:10.1016/0031-9201(77)90108-X.

Dunlop, D. J. (2002), Theory and application of the Day plot (M_{rs}/M_s versus H_{cr}/H_c): 1. Theoretical curves and tests using titanomagnetite data, *J. Geophys. Res.*, *107*(B3), 2056, doi:10.1029/2001JB000486.

Egli, R. (2004a), Characterization of individual rock magnetic components by analysis of remanence curves, 1. Unmixing natural sediments, *Stud. Geophys. Geod.*, *48*, 391–446, doi:10.1023/B:SGEG.0000020839.45304.6d.

Egli, R. (2004b), Characterization of individual rock magnetic components by analysis of remanence curves. 2. Fundamental properties of coercivity distributions, *Phys. Chem. Earth*, *29*, 851–867, doi:10.1016/S1474-7065(04)00129-9.

Egli, R. (2004c), Characterization of individual rock magnetic components by analysis of remanence curves. 3. Bacterial magnetite and natural processes in lakes, *Phys. Chem. Earth*, *29*, 869–884, doi:10.1016/j.pce.2004.03.010.

Egli, R. (2006a), Theoretical considerations on the anhysteretic remanent magnetization of interacting particles with uniaxial anisotropy, *J. Geophys. Res.*, *111*, B12S18, doi:10.1029/2006JB004577.

Egli, R. (2006b), Theoretical aspects of dipolar interactions and their appearance in first-order reversal curves of thermally activated single-domain particles, *J. Geophys. Res.*, *111*, B12S17, doi:10.1029/2006JB004567.

Egli, R., A. P. Chen, M. Winklhofer, K. P. Kodama, and C. S. Horng (2010), Detection of noninteracting single domain particles using first-order reversal curve diagrams, *Geochem. Geophys. Geosyst.*, *11*, Q01Z11, doi:10.1029/2009GC002916.

Faivre, D., and D. Schüler (2008), Magnetotactic bacteria and magnetosomes, *Chem. Rev.*, *108*, 4875–4898, doi:10.1021/cr078258w.

Fischer, H., G. Mastrogiacomo, J. F. Löffler, R. J. Warthmann, P. G. Weidler, and A. U. Gehring (2008), Ferromagnetic resonance and magnetic characteristics of intact magnetosome chains in *Magnetospirillum gryphiswaldense*, *Earth Planet. Sci. Lett.*, *270*, 200–208, doi:10.1016/j.epsl.2008.03.022.

Flies, C. B., H. M. Jonkers, D. de Beer, K. Bosselmann, M. E. Böttcher, and D. Schüler (2005), Diversity and vertical distribution of magnetotactic bacteria along chemical gradients in freshwater microcosms, *FEMS Microbiol. Ecol.*, *52*, 185–195, doi:10.1016/j.femsec.2004.11.006.

Gehring, A. U., J. Kind, M. Charilaou, and I. García-Rubio (2011), The detection of magnetotactic bacteria and magnetofossils by means of magnetic anisotropy, *Earth Planet. Sci. Lett.*, *309*, 113–117, doi:10.1016/j.epsl.2011.06.024.

Harrison, R. J., and J. M. Feinberg (2008), FORCinel: An improved algorithm for calculating first-order reversal curve distributions using locally weighted regression smoothing, *Geochem. Geophys. Geosyst.*, *9*, Q05016, doi:10.1029/2008GC001987.

Hesse, P. P. (1994), Evidence for bacterial paleoecological origin of mineral magnetic cycles in oxic and sub-oxic Tasman Sea sediments, *Mar. Geol.*, *117*, 1–17, doi:10.1016/0025-3227(94)90003-5.

Housen, B. A., and B. M. Moskowitz (2006), Depth distribution of magnetofossils in near-surface sediments from the Blake/Bahama Outer Ridge, western North Atlantic Ocean, determined by low-temperature magnetism, *J. Geophys. Res.*, *111*, G01005, doi:10.1029/2005JG000068.

Jackson, M., and P. Solheid (2010), On the quantitative analysis and evaluation of magnetic hysteresis data, *Geochem. Geophys. Geosyst.*, *11*, Q04Z15, doi:10.1029/2009GC002932.

Jimenez-Lopez, C., C. S. Romanek, and D. A. Bazylinski (2010), Magnetite as a prokaryotic biomarker: A review, *J. Geophys. Res.*, *115*, G00G03, doi:10.1029/2009JG001152.

Johnson, H. P., W. Lowrie, and D. V. Kent (1975), Stability of anhysteretic remanent magnetization in fine and coarse magnetite and maghemite particles, *Geophys. J. R. Astron. Soc.*, *41*, 1–10, doi:10.1111/j.1365-246X.1975.tb05480.x.

Kim, B., K. Kodama, and R. Moeller (2005), Bacterial magnetite produced in water column dominates lake sediment mineral magnetism: Lake Ely, USA, *Geophys. J. Int.*, *163*, 26–37, doi:10.1111/j.1365-246X.2005.02735.x.

Kind, J., A. U. Gehring, M. Winklhofer, and A. M. Hirt (2011), Combined use of magnetometry and spectroscopy for identifying magnetofossils in sediments, *Geochem. Geophys. Geosyst.*, *12*, Q08008, doi:10.1029/2011GC003633.

King, J., S. K. Banerjee, J. Marvin, and Ö. Özdemir (1982), A comparison of different magnetic methods for determining the relative grain size of magnetite in natural materials: Some results from lake sediments, *Earth Planet. Sci. Lett.*, *59*, 404–419, doi:10.1016/0012-821X(82)90142-X.

Kobayashi, A., J. L. Kirschvink, C. Z. Nash, R. E. Kopp, D. A. Sauer, L. E. Bertani, W. F. Voorhout, and T. Taguchi (2006), Experimental observation of magnetosome chain collapse in magnetotactic bacteria: Sedimentological, paleomagnetic, and evolutionary implications, *Earth Planet. Sci. Lett.*, *245*, 538–550, doi:10.1016/j.epsl.2006.03.041.

Kopp, R. E., and J. L. Kirschvink (2008), The identification and biogeochemical interpretation of fossil magnetotactic bacteria, *Earth Sci. Rev.*, *86*, 42–61, doi:10.1016/j.earscirev.2007.08.001.

Kopp, R. E., C. Z. Nash, A. Kobayashi, B. P. Weiss, D. A. Bazylinski, and J. L. Kirschvink (2006a), Ferromagnetic resonance spectroscopy for assessment of magnetic anisotropy and magnetostatic interactions: A case study of mutant magnetotactic bacteria, *J. Geophys. Res.*, *111*, B12S25, doi:10.1029/2006JB004529.

Kopp, R. E., B. P. Weiss, A. C. Maloof, H. Vali, C. Z. Nash, and J. L. Kirschvink (2006b), Chains, clumps, and strings: Magnetofossil taphonomy with ferromagnetic resonance spectroscopy, *Earth Planet. Sci. Lett.*, *247*, 10–25, doi:10.1016/j.epsl.2006.05.001.

Kopp, R. E., T. D. Raub, D. Schumann, H. Vali, A. V. Smirnov, and J. L. Kirschvink (2007), Magnetofossil spike during the Paleocene-Eocene thermal maximum: Ferromagnetic resonance, rock magnetic, and electron microscopy evidence from Ancora, New Jersey, United States, *Paleoceanography*, *22*, PA4103, doi:10.1029/2007PA001473.

Kopp, R. E., D. Schumann, T. D. Raub, D. S. Powars, L. V. Godfrey, N. L. Swanson-Hysell, A. C. Maloof, and H. Vali (2009), An Appalachian Amazon? Magnetofossil evidence for the development of a tropical river-like system in the mid-Atlantic United States during the Paleocene-Eocene thermal maximum, *Paleoceanography*, *24*, PA4211, doi:10.1029/2009PA001783.

Larrasoaña, J. C., A. P. Roberts, L. Chang, S. A. Schellenberg, J. D. Fitz Gerald, R. D. Norris, and J. C. Zachos (2012), Magnetotactic bacterial response to Antarctic dust supply during the Palaeocene–Eocene thermal maximum, *Earth Planet. Sci. Lett.*, *333–334*, 122–133, doi:10.1016/j.epsl.2012.04.003.

Li, J. H., and Y. X. Pan (2012), Environmental factors affect magnetite magnetosome synthesis in *Magnetospirillum magneticum* AMB-1: Implications for biologically controlled mineralization, *Geomicrobiol. J.*, *29*, 362–373, doi:10.1080/01490451.2011.565401.

Li, J. H., Y. X. Pan, G. J. Chen, Q. S. Liu, L. X. Tian, and W. Lin (2009), Magnetite magnetosome and fragmental chain formation of *Magnetospirillum magneticum* AMB-1: Transmission electron microscopy and magnetic observations, *Geophys. J. Int.*, *177*, 33–42, doi:10.1111/j.1365-246X.2009.04043.x.

Li, J. H., Y. X. Pan, Q. S. Liu, H. F. Qin, C. L. Deng, R. C. Che, and X. A. Yang (2010a), A comparative study of magnetic properties between whole cells and isolated magnetosomes of *Magnetospirillum magneticum* AMB-1, *Chin. Sci. Bull.*, *55*, 38–44, doi:10.1007/s11434-009-0333-x.

Li, J. H., et al. (2010b), Biomineralization, crystallography and magnetic properties of bullet-shaped magnetite magnetosomes in giant rod magnetotactic bacteria, *Earth Planet. Sci. Lett.*, *293*, 368–376, doi:10.1016/j.epsl.2010.03.007.

Lin, W., and Y. X. Pan (2009), Uncultivated magnetotactic cocci from Yuandadu Park in Beijing, China, *Appl. Environ. Microbiol.*, *75*, 4046–4052, doi:10.1128/AEM.00247-09.

Lin, W., Y. Z. Wang, B. Li, and Y. X. Pan (2012), A biogeographic distribution of magnetotactic bacteria influenced by salinity, *ISME J.*, *6*, 475–479, doi:10.1038/ismej.2011.112.

Moskowitz, B. M., R. B. Frankel, P. J. Flanders, R. P. Blakemore, and B. B. Schwartz (1988), Magnetic properties of magnetotactic bacteria, *J. Magn. Magn. Mater.*, *73*, 273–288, doi:10.1016/0304-8853(88)90093-5.

Moskowitz, B. M., R. B. Frankel, and D. A. Bazylinski (1993), Rock magnetic criteria for the detection of biogenic magnetite, *Earth Planet. Sci. Lett.*, *120*, 283–300, doi:10.1016/0012-821X(93)90245-5.

Moskowitz, B. M., D. A. Bazylinski, R. Egli, R. B. Frankel, and K. J. Edwards (2008), Magnetic properties of marine magnetotactic bacteria in a seasonally stratified coastal pond (Salt Pond, MA, USA), *Geophys. J. Int.*, *174*, 75–92, doi:10.1111/j.1365-246X.2008.03789.x.

Paasche, Ø., and R. Løvlie (2011), Synchronized postglacial colonization by magnetotactic bacteria, *Geology*, *39*, 75–78, doi:10.1130/G31525.1.

Pan, Y. X., N. Petersen, A. F. Davila, L. M. Zhang, M. Winklhofer, Q. S. Liu, M. Hanzlik, and R. X. Zhu (2005a), The detection of bacterial magnetite in recent sediments of Lake Chiemsee (southern Germany), *Earth Planet. Sci. Lett.*, *232*, 109–123, doi:10.1016/j.epsl.2005.01.006.

Pan, Y. X., N. Petersen, M. Winklhofer, A. F. Davila, Q. S. Liu, T. Frederichs, M. Hanzlik, and R. X. Zhu (2005b), Rock magnetic properties of uncultured magnetotactic bacteria, *Earth Planet. Sci. Lett.*, *237*, 311–325, doi:10.1016/j.epsl.2005.06.029.

Passier, H. F., and M. J. Dekkers (2002), Iron oxide formation in the active oxidation front above sapropel S1 in the eastern Mediterranean Sea as derived from low-temperature magnetism, *Geophys. J. Int.*, *150*, 230–240, doi:10.1046/j.1365-246X.2002.01704.x.

Petermann, H., and U. Bleil (1993), Detection of live magnetotactic bacteria in South Atlantic deep-sea sediments, *Earth Planet. Sci. Lett.*, *117*, 223–228, doi:10.1016/0012-821X(93)90128-V.

Petersen, N., T. Von Dobeneck, and H. Vali (1986), Fossil bacterial magnetite in deep-sea sediments from the South Atlantic Ocean, *Nature*, *320*, 611–615, doi:10.1038/320611a0.

Pike, C. R., A. P. Roberts, and K. L. Verosub (1999), Characterizing interactions in fine magnetic particle systems using first order reversal curves, *J. Appl. Phys.*, *85*, 6660–6667, doi:10.1063/1.370176.

Pike, C. R., A. P. Roberts, and K. L. Verosub (2000), The effect of magnetic interactions on low temperature saturation remanence in fine magnetic particle systems, *J. Appl. Phys.*, *88*, 967–974, doi:10.1063/1.373763.

Preisach, F. (1935), Über die magnetische Nachwirkung, *Z. Phys.*, *94*, 277–302, doi:10.1007/BF01349418.

Roberts, A. P., C. R. Pike, and K. L. Verosub (2000), First-order reversal curve diagrams: A new tool for characterizing the magnetic properties of natural samples, *J. Geophys. Res.*, *105*(B12), 28,461–28,475, doi:10.1029/2000JB900326.

Roberts, A. P., F. Florindo, G. Villa, L. Chang, L. Jovane, S. M. Bohaty, J. C. Larrasoaña, D. Heslop, and J. D. Fitz Gerald (2011), Magnetotactic bacterial abundance in pelagic marine environments is limited by organic carbon flux and availability of dissolved iron, *Earth Planet. Sci. Lett.*, *310*, 441–452, doi:10.1016/j.epsl.2011.08.011.

Roberts, A. P., L. Chang, D. Heslop, F. Florindo, and J. C. Larrasoaña (2012), Searching for single domain magnetite in the "pseudo-single-domain" sedimentary haystack: Implications of biogenic magnetite preservation for sediment magnetism and relative paleointensity determinations, *J. Geophys. Res.*, *117*, B08104, doi:10.1029/2012JB009412.

Schumann, D., et al. (2008), Gigantism in unique biogenic magnetite at the Paleocene-Eocene Thermal Maximum, *Proc. Natl. Acad. Sci. U. S. A.*, *105*, 17,648–17,653, doi:10.1073/pnas.0803634105.

Shaw, J. (1974), A new method of determining the magnitude of the palaeomagnetic field: Application to five historic lavas and five archaeological samples, *Geophys. J. R. Astron. Soc.*, *39*, 133–141, doi:10.1111/j.1365-246X.1974.tb05443.x.

Simmons, S. L., S. M. Sievert, R. B. Frankel, D. A. Bazylinski, and K. J. Edwards (2004), Spatiotemporal distribution of marine magnetotactic bacteria in a seasonally stratified coastal salt pond, *Appl. Environ. Microbiol.*, *70*, 6230–6239, doi:10.1128/AEM.70.10.6230-6239.2004.

Smirnov, A. V., and J. A. Tarduno (2000), Low-temperature magnetic properties of pelagic sediments (Ocean Drilling Program Site 805C): Tracers of maghemitization and magnetic

mineral reduction, *J. Geophys. Res.*, *105*(B7), 16,457–16,471, doi:10.1029/2000JB900140.

Sugiura, N. (1979), ARM, TRM and magnetic interactions: Concentration dependence, *Earth Planet. Sci. Lett.*, *42*, 451–455, doi:10.1016/0012-821X(79)90054-2.

Thomas-Keprta, K. L., S. J. Clemett, D. A. Bazylinski, J. L. Kirschvink, D. S. McKay, S. J. Wentworth, H. Vali, E. K. Gibson, and C. S. Romanek (2002), Magnetofossils from ancient Mars: A robust biosignature in the Martian meteorite ALH84001, *Appl. Environ. Microbiol.*, *68*, 3663–3672, doi:10.1128/AEM.68.8.3663-3672.2002.

Walz, F. (2002), The Verwey transition-A topical review, *J. Phys.*, *14*, R285, doi:10.1088/0953-8984/14/12/203.

Weiss, B. P., S. S. Kim, J. L. Kirschvink, R. E. Kopp, M. Sankaran, A. Kobayashi, and A. Komeili (2004a), Ferromagnetic resonance and low-temperature magnetic tests for biogenic magnetite, *Earth Planet. Sci. Lett.*, *224*, 73–89, doi:10.1016/j.epsl.2004.04.024.

Weiss, B. P., S. S. Kim, J. L. Kirschvink, R. E. Kopp, M. Sankaran, A. Kobayashi, and A. Komeili (2004b), Magnetic tests for magnetosome chains in Martian meteorite ALH84001, *Proc. Natl. Acad. Sci. U. S. A.*, *101*, 8281–8284, doi:10.1073/pnas.0402292101.

Winklhofer, M., and G. T. Zimanyi (2006), Extracting the intrinsic switching field distribution in perpendicular media: A comparative analysis, *J. Appl. Phys.*, *99*, 08E710, doi:10.1063/1061.2176598.

Yamazaki, T. (2012), Paleoposition of the Intertropical Convergence Zone in the eastern Pacific inferred from glacial-interglacial changes in terrigenous and biogenic magnetic mineral fractions, *Geology*, *40*, 151–154, doi:10.1130/G32646.1.

Yamazaki, T., and H. Kawahata (1998), Organic carbon flux controls the morphology of magnetofossils in marine sediments, *Geology*, *26*, 1064–1066, doi:10.1130/0091-7613(1998)026<1064:OCFCTM>2.3.CO;2.

Yu, Y. (2010), Paleointensity determination using anhysteretic remanence and saturation isothermal remanence, *Geochem. Geophys. Geosyst.*, *11*, Q02Z12, doi:10.1029/2009GC002804.

Zhu, K. L., et al. (2010), Isolation and characterization of a marine *magnetotactic spirillum* axenic culture QH-2 from an intertidal zone of the China Sea, *Rev. Microbiol.*, *161*, 276–283.